Undersizing of Aged African Biomass Burning Aerosol by an Ultra High Sensitivity Aerosol Spectrometer

Steven G. Howell[1], Steffen Freitag[1], Amie Dobracki[1,2], Nikolai Smirnow[1,3], and Arthur J. Sedlacek III[4]

[1]University of Hawaii at Manoa, Department of Oceanography, Honolulu, HI USA
[2]Now at Rosenstiel School of Marine and Atmospheric Science, University of Miami, Miami, FL USA
[3]Now at NetApp, Boulder, CO USA
[4]Brookhaven National Laboratory, US Department of Energy, Upton, NY USA

Correspondence: Steven Howell (sghowell@hawaii.edu)

Abstract. The Ultra-High Sensitivity Aerosol Spectrometer (UHSAS) differs from most other optical particle spectrometers by using a high-power infrared (IR) laser to detect small particles and reduce the sizing ambiguity due to the non-monotonicity of scattering with particle size.

During the NASA ORACLES project (ObseRvations of Aerosols above CLouds and their intEractionS) over the southeast
5 Atlantic Ocean, the UHSAS clearly undersized particles in the biomass burning plume extending from Southern Africa. Since the horizontal and vertical extent of the plume was vast, the NASA P-3B research aircraft often flew through a fairly uniform biomass burning plume for periods exceeding 30 minutes, sufficient time to explore the details of the UHSAS response by selecting single particle sizes with a Differential Mobility Analyzer (DMA) and passing them to the UHSAS. This was essentially an in-flight calibration of the UHSAS using the particles of interest. Two modes of responses appeared. Most particles
10 were undersized by moderate amounts, ranging from not at all for 70 nm aerosols to 15 % for 280 nm particles. Mie scattering calculations show that composition-dependent refractive index of the particles is unlikely to explain the pattern. Heating of brown carbon or tarballs in the beam causing evaporation and shrinking of the particles is the most plausible explanation, though that requires greater IR absorption than is usually attributed to brown carbon. 10–30 % of the particles were undersized by 25 to 35 %. Those were apparently the particles containing refractory black carbon. Laboratory calibrations confirm that
15 black carbon is drastically undersized by the UHSAS, though the mechanism is not entirely clear.

A simple empirical correction equation was implemented that dramatically improves agreement with DMA distributions between 100 and 500 nm. It raised median particle diameter 18 nm, from 163 to 181 nm during the August 2017 deployment and by smaller amounts during deployments with less intense pollution. Calculated scattering from UHSAS size distributions increased by about 130 %, dramatically improving agreement with scattering measured by nephelometers. The correction is
20 only valid in polluted instances; clean marine boundary layer and free troposphere aerosols behaved more like the calibration spheres. We were unable to directly test the correction between 500 and 1000 nm, though APS data appear to show that the correction is poor at the largest diameters, which is no surprise as the composition of those particles is likely to be quite different than that of the accumulation mode. This adds to the evidence that UHSAS data must be treated cautiously whenever the aerosol may absorb infrared light. Similar corrections may be required whenever brown carbon aerosol is present.

1 Introduction

Particles in the air, or aerosols, play a major role in the atmosphere. They directly affect the radiation balance of the Earth by scattering sunlight, and indirectly by affecting cloud properties (Twomey, 1977; Albrecht, 1989; Boucher et al., 2013). They participate in geochemical cycling of nutrients (e.g., Chadwick et al., 1999) and pollutants, and can have negative impacts on

30   human health (e.g., Woodcock, 1948; Shiraiwa et al., 2017; Burnett et al., 2018).

The wide span of aerosol sizes (from $< 1\,\mathrm{nm}$ to $> 100\,\mathrm{\mu m}$), composition, and shapes mean there is no wholly satisfactory method of measuring particle size. In the case of non-spherical particles, there is not even a single definition of diameter that is universally applicable (Baron and Willeke, 1993).

Optical particle counters (OPCs) that work by measuring individual particle scattering from a light beam are appealing

35   because they can have high size resolution and rapidly size particles in the diameter ranges that most affect health, radiation, and cloud properties. A wide variety of these instruments have been used in field projects over the last few decades (e.g., Whitby and Vomela, 1967; Clarke, 1991; Gebhart, 1993; Ames et al., 2000; Hand and Kreidenweis, 2002; Haywood et al., 2003; McNaughton et al., 2009; Rosenberg et al., 2012). The main drawback is that the amount of scattered light detected by an OPC is affected by particle shape, composition, inhomogeneities, wavelength of light, and the angles between particle, light

40   beam, and the detection optics. To make matters worse, even in the ideal case, with homogeneous spheres of known refractive index, resonances between the light waves and the particles mean that the amount of light scattered is non-monotonic with diameter for particles near the wavelength of light.

There are a few ways to mitigate these resonances, sometimes called "Mie wiggles", after Gustav Mie, who first solved the problem of light scattering due to arbitrary diameter homogeneous spheres (Mie, 1908). One can use white light (Chen

45   et al., 1984; Liu et al., 1985); concentrate on forward scattering, where Mie wiggles are reduced (Gebhart, 1991); do inversions to rationally assign particles with a given scattering to appropriate sizes (Ames et al., 2000; Wang, 2002; Rosenberg et al., 2012); smooth the response curve (e.g., Robinson and Lamb, 1986; Clarke, 1991) or broaden the size bins to accommodate the uncertainty.

This uncertainty is particularly pronounced when trying to calculate higher moments, such as surface area or particle mass.

50   Since those vary with the square and cube of diameter, small errors in sizing are magnified considerably. One can partially compensate by determining how scattering would be affected by a refractive index calculated from particle composition, but the fundamental ambiguity remains.

1.1 The UHSAS

Droplet Measurement Technology's Ultra-High Sensitivity Aerosol Spectrometer (UHSAS) (Cai et al., 2008) approaches this

55   problem by using infrared (IR) light (1054 nm), keeping Mie scattering monotonic through the UHSAS maximum diameter of 1000 nm and meaning particles below 300 nm are within the Rayleigh regime, where scattering goes with the 6th power of

diameter, giving a nice log-linear relationship over much of the sizing range. This has the additional benefit of suppressing the effect of shape: when the particle size is much smaller than wavelength, scattering is determined primarily by the volume of the particle rather than the cross section (Gebhart, 1993). It requires an intense laser to detect the smallest particles ($\sim 1\,\mathrm{kW}$

60   circulating in the sample volume) and wide-ranging amplification to handle the > 6 orders of magnitude scattering change over the 60 to 1000 nm nominal detection limits. To achieve this, the UHSAS uses a pair of detectors, one an avalanche photodiode and the other a low gain PIN photodiode. Each photodiode has two output channels with different gains, yielding 4 channels spanning the range of particle scattering.

As with any optical particle sizer, the UHSAS is subject to sizing errors when the refractive index of sample particles is

65   different than that of the calibration material. One can approach that by using calibration materials close to the refractive index of natural aerosol (Sawamura et al., 2017), use Mie scattering calculations and composition to correct calibrations for sampled aerosol (Ames et al., 2000; Cai et al., 2008), or conclude that the errors are small enough to ignore (Volkamer et al., 2015). But it appears that the UHSAS may have unique problems with black carbon. Yokelson et al. (2011) noted poor behavior of the UHSAS in a Mexican biomass burning (BB) plume and concluded that strongly absorbing particles are essentially invisible to

70   the UHSAS.

1.2   A note about black carbon

Light absorbing carbonaceous material (LAC) is one of the most difficult parts of aerosol to describe chemically, to measure, and to model (Bond and Bergstrom, 2006). It is poorly defined chemically, tends to be highly aspherical, and is present in highly variable quantities. The plethora of names invented to describe it gives an indication of the complexity: soot, elemental

75   carbon (EC), black carbon (BC), refractory black carbon (rBC), brown carbon (BrC), and tarballs all address subtly different properties. Historically, it has been practical to measure either the amount of carbon with chemical methods or the blackness with absorption measurements, but quantitatively connecting the two remains a challenge.

A review of this is beyond the scope of this paper, but a description of how the terms are used in this paper may be useful. rBC refers to the LAC detected by a DMT Single Particle Soot Photometer (SP2), which heats IR-absorbing particles to boiling,

80   roughly 4000 K for graphite. That clearly includes graphitic material and amorphous carbon, but also other carbonaceous species that char and form rBC as they heat (Sedlacek et al., 2018b). BC is a hypothetical material that absorbs more or less as a black body and includes graphitic soot nanospheres and amorphous C. BrC is organic material that absorbs light primarily at short wavelengths (Andreae and Gelencser, 2006) and to a small and very poorly known extent in the IR (e.g. Li et al., 2020; Sumlin et al., 2018b). Tarballs (Pósfai et al., 2003, 2004) are a distinctively spherical variety of BrC prevalent in aged biomass

85   burning plumes. Their optical properties are also poorly known, though it appears that they may absorb more in the IR than other BrC (Alexander et al., 2008; Hoffer et al., 2017; Sedlacek et al., 2018a).

1.3   ORACLES (ObseRvations of Aerosols above CLouds and their intEractionS)

ORACLES was a NASA-funded project to examine the direct, indirect, and semi-direct influence of aerosol from burning fields in Africa on the radiative balance over the southeast Atlantic Ocean (Redemann et al., 2020). It was an aircraft-based project

90   with field deployments in September 2016, August 2017, and October 2018. The NASA P-3B was deployed each year, with an extensive payload of aerosol, cloud droplet, radiation, and remote sensors. See https://espo.nasa.gov/oracles for a project description and links to data and other publications.

The Hawaii Group for Environmental Aerosol Research deployed a UHSAS in addition to a set of Differential Mobility Analyzers (DMAs) to take advantage of the superior time resolution of the UHSAS (1 s or less compared with 90 s), particularly

95   valuable during vertical profiles and when sampling in and around clouds. The UHSAS also offered detection limits of 60 nm, sufficient to detect nearly all particles likely to activate within clouds.

Aerosol in the ORACLES project was largely aged smoke from burning fields and forests in southern Africa. Plume ages were typically 2 days to 2 weeks, and the aerosol was dominated by organic material with substantial rBC. Data from the first two years showed that when compared to size distributions from the DMAs the UHSAS consistently sized particles too small.

100 During the final year, we installed tubing and valves to allow a UHSAS to sample size-selected particles from a DMA during flight. This allowed us to directly test any sizing anomalies due to the characteristics of the ambient aerosol. It was essentially an in-flight UHSAS calibration using particles representative of the plume. This kind of calibration while sampling is not new, as Stolzenburg et al. (1998) did essentially the same thing, but it is the first aircraft deployment we are aware of in a biomass burning plume. We also anticipated that by measuring scattering from aerosol of known size, we could determine refractive

105 index as was done by Hand and Kreidenweis (2002), but on a single-particle basis.

This test was only possible because the plume we were studying was vast (Pistone et al., 2019; Redemann et al., 2020; Shinozuka et al., 2020); we often spent a half hour or more in remarkably constant aerosol. This is normally impractical with fast-moving aircraft ($\sim$100 ms^{-1}) even considerably downwind of a fire.

2   Methods

110 In the lab and in the field, all sizing instruments were calibrated with polystyrene latex (PSL) spheres (real refractive index $n = 1.572$ at the UHSAS laser wavelength) from 70 to 800 nm diameter. DMA high voltage amplifiers and flow rates were checked regularly between PSL calibrations.

2.1   Lab Tests

In addition to the field deployment, we tested various materials in the laboratory, partly to familiarize ourselves with the

115 UHSAS, but also to explore the sizing problems evident in the first 2 years. It was not practical to generate good proxies for the aged BB particles present in the field, so we tested some representative non-absorbing salts (NaCl, Na_2SO_4, and H_2SO_4) and some strongly-absorbing materials containing refractory black carbon (rBC) (Aquadag, a suspension of graphite particles, and fullerene soot, which is $\sim$90 % amorphous black carbon and $\sim$10 % fullerene, chiefly the C_{60} form (Gysel et al., 2011).)

Aerosol materials were tested by nebulizing aqueous solutions of the material of interest, mixing in dry air to reduce relative

120 humidity (RH) below 30 % to evaporate water from the particles, passing the particles through a long DMA (LDMA), and then into the UHSAS. The LDMA was a modified TSI 3071A; essentially only the DMA column remains; flow control, neutralizers,

high-voltage amplifiers, and software have all been replaced. The LDMA sheath air was desiccated, so particles were selected at < 5 % RH. For the Fullerene and Aquadag tests, sample air was heated to 450°C in a tube furnace to remove any volatile material before entering the DMA. Gysel et al. (2011) tested Aquadag aerosol passing through a thermal denuder operating at
125   400°C and found that it effectively removed organic carbon, leaving particles that were $\sim$87 % rBC by mass.

DMAs classify particles by the balance between electrostatic attraction and air resistance, so cannot tell the difference between a singly charged particle of a given size and a doubly or even triply charged particle with twice or thrice the drag. While this is a complication when inverting DMA data into size distributions, it is useful when calibrating an OPC, as the multiply charged particles show up as separate peaks in the distribution. This has the effect of extending the calibrations to
130   diameters that are in a sense greater than the DMA can select. In the lab, triply charged peaks were sometimes distinct enough to be useful, and double charges were sufficient to extend the testing to 1083 nm from the 600 nm maximum selection diameter we used.

2.2   Using the UHSAS in ORACLES

The aerosol sizing package aboard the NASA P-3B during ORACLES included two DMA systems, the UHSAS, a TSI 3321
135   Aerodynamic Particle Sizer (APS), and DMT SP2. In addition, a pair of TSI 3563 3-wavelength nephelometers measured aerosol light scattering, which is strongly related to particle size. The second nephelometer was in series with the first and a 1 μm aerodynamic diameter impactor was periodically switched in between them. Sample air for all instruments was drawn through a shrouded inlet that samples aerosol particles with near 100 % efficiency to roughly 3 μm (McNaughton et al., 2007).

Both DMA units used grab samplers (Clarke et al., 1998) to ensure constant size distributions through the 60 second scans.
140   Modified versions of the software developed by Zhou (2001) controlled the systems and inverted the size distributions. One of the units was the modified TSI 3071 LDMA mentioned above. The other was a thermal tandem DMA system (TDMA) that used a nano-DMA (TSI 3085) and a radial DMA (RDMA) (Zhang et al., 1995) and could be configured to scan with either DMA or select a mobility size with one DMA and scan the resulting particles with the other either directly or after heating to 300°C (Clarke et al., 2004). Sample air was not dried, but excess air from each DMA was desiccated and recycled as sheath
145   air, so particles in the DMA were rapidly dried as they migrated through the sheath air and sizing was effectively at low RH.

The UHSAS operated in slightly different configurations each year. In 2016, sample air was either unheated or passed through a 400°C thermal denuder that eliminated volatile material (Clarke, 1991). The valve system suffered from diffusion losses of small particles, so an empirical diameter-dependent correction was implemented by comparison with the long DMA. The denuder was absent in 2017, but reintroduced in 2018 (though the volatility data are not explored here). In 2017, sample
150   flow to the UHSAS was diluted 50:50 with desiccated zero air to ensure a low RH, reducing particle growth due to liquid water to a minimum. High RH was only rarely a problem, and only in the marine boundary layer, as the FT had low water vapor content and sample air was heated to cabin temperature.

In 2018 the thermal denuder and desiccated dilution flow were used, and as mentioned above, a system was installed to divert size-selected particles from the TDMA to the UHSAS. The dilution flow system was bypassed during this mode of operation as
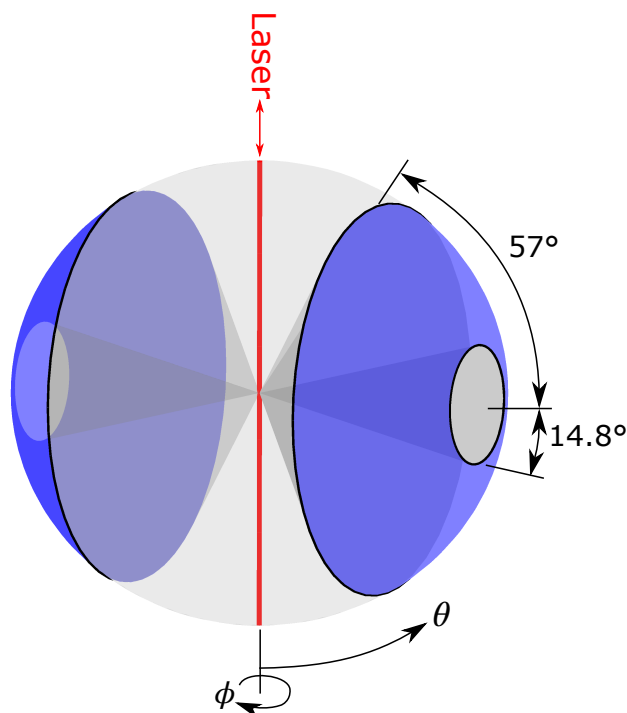
Figure 1. Scattering angles detected by the UHSAS. Mangin mirrors on opposite sides of the laser focus scattered light on the detectors from annular regions perpendicular to the beam between 14.8° and 57°(shown as the blue surface). The Mie routines calculate scattering integrated over angles θ (away from the beam) and ϕ (relative to the laser polarization) and integrate over the sensing region.

155 RH was already low from the TDMA. The largest particles the RDMA could select at altitude were 180 nm; the LDMA could select 500 nm particles, but was about 4 m away from the UHSAS, so it was not practical to use for the in-flight calibration.

2.3 Scattering calculations for the UHSAS

In the UHSAS, scattered light is focused on detectors on opposite sides of the scattering region. Each uses a identical set of optics consisting of a pair of Mangin mirrors that accept light scattered in an annular region between 14.8° and 57.0° from

160 perpendicular to the beam (Fig. 1). There must also be a direct 90° scattering path from the particle to the detectors that bypasses the mirrors, but that is a trivial fraction of the collected light and is ignored in these calculations. Laser light is linearly polarized with the electric field parallel to the particle beam and perpendicular to the axis of the collection optics (Droplet Measurement Technologies, 2013).

Mie scattering calculations were performed with Matlab code derived from the FORTRAN programs in Wickramasinghe

165 (1973) and checked against other libraries, including Bohren and Huffman (1983) and PyMieScat (Sumlin et al., 2018a). Appendix A has some details about how the calculations were done.
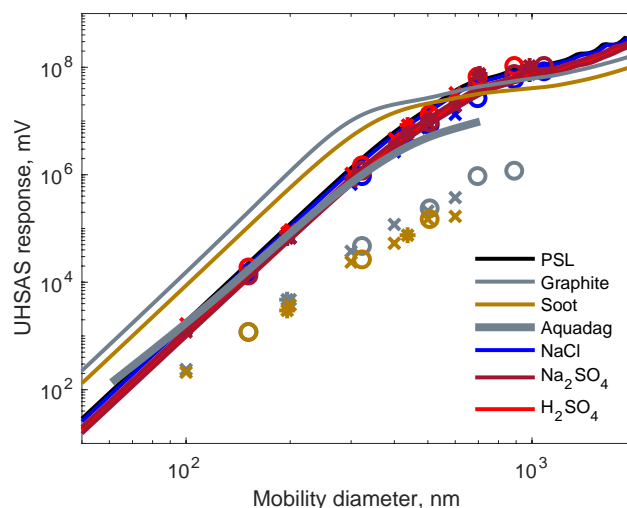
Figure 2. Mie calculations over the collection angles of the UHSAS for particles with various refractive indexes and observed responses. Spherical, homogeneous particles are assumed. Symbols represent measured response from particles sized with a long DMA. '×' are singly charged, '○ are doubly charged, and '∗' are triply charged particles. For test particles the y axis is the signal from the peak height detector. For the theoretical curves it is V from Eq. A7 with C_{opt} determined from the peak height of sub-300 μm PSL calibration spheres.
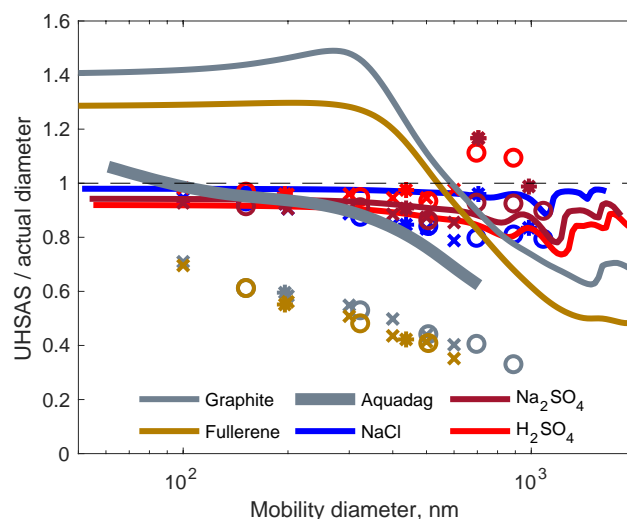
Figure 3. The same data as Fig. 2, but the y axis is the ratio of theoretical UHSAS response (lines) or measurements (symbols) to that of PSL spheres.

Calculated UHSAS response to several types of particles are shown as lines in Fig. 2. Table 1 shows the corresponding refractive indices. The non-absorbing materials have slightly lower n than PSL so they lie just underneath the almost completely hidden PSL trace. In contrast, spheres of amorphous soot and graphite (often used as surrogates for aerosol BC) have elevated
170   n and k, and scatter far more light up to about 600 nm.

However, actual BC particles are rarely spheres. As a crude attempt at a more realistic scattering calculation, we show a curve for Aquadag, a graphitic material previously used to calibrate SP2s. Aquadag particles are not solid; they tend to be a jumble of minuscule graphite plates. When size-selected by a DMA, their asphericity increases aerodynamic resistance so the rBC mass of the particle is smaller than would be expected. Gysel et al. (2011) established an effective density relationship
175   between mobility diameter from the DMA and mass of BC. Particles are modeled here as homogeneous spheres with volume weighted refractive index of graphite and air using mixing rules from Liu and Daum (2008). This simple modeling predicts that Aquadag particles (the black line in Figs. 2 and 3) should scatter similarly to the non-absorbing materials rather than like pure graphite.

Fullerene soot is morphologically quite distinct from Aquadag, with fractal-like soot amidst occasional carbon nanospheres,
180   chiefly the C_{60} form of fullerene. However, the effect on DMA sizing is similar, and Gysel et al. (2011) also determined an effective density for fullerene soot aerosol. The resulting curve is almost atop the Aquadag one, so is not shown on the figure. Since neither graphite, soot, nor fullerene are homogeneous spheres, this calculation is intended as a really crude approximation, not as a quantitative prediction of expected behavior.

Fig. 3 shows the same scattering calculations recast to show how much bigger or smaller particles of different materials
185   would appear when using a PSL calibration. This magnifies the difference between curves so one can see the complex behavior for particle diameters near the wavelength of the UHSAS laser.

3   Results and Discussion

3.1   Lab Results

The symbols in Figs. 2 and 3 show the results of the lab tests. In general, the non-absorbing materials follow the expected
190   curves fairly closely, though at diameters above the Rayleigh scattering regime, the data are a bit noisy, due to non-spherical salt particles, Mie wiggles, and poor statistics for the doubly and triply charged particles.

In contrast, the two varieties of black carbon scatter far less light than expected, from an order of magnitude for small particles to a factor of 100 for the largest particles. This results in undersizing from 30 % at 100 nm to 67 % at 900nm. Dramatic undersizing of absorbing particles by OPCs has been noted before (Whitby and Vomela, 1967), but those were for
195   particles much larger than the wavelength and the undersizing was predicted from Mie theory. (In their case, the undersizing was not as extreme as predicted, which they attributed to non-sphericity.)

One possible reason for this discrepancy is that particles shrink while heated by the UHSAS laser. Cai et al. (2008) calculated that heating in the UHSAS beam was insufficient to significantly shrink particles of NH_4NO_3, which are quite volatile, but absorb IR light very weakly. They confirmed that the UHSAS sized NH_4NO_3 accurately. They did not address the far higher

Table 1. Refractive indices near 1054 nm

Species	Refractive index
PSL	1.572
H_2SO_4[a]	$1.426 - 1.36 \times 10^{-6}i$
NaCl[b]	1.5314
NH_4NO_3[c]	$1.57 - 2 \times 10^{-6}i$
Na_2SO_4[d]	1.468
graphite[e]	$3.2397 - 2.0233i$
soot[f]	$2.26 - 1.26i$
amorphous C[f]	$2 - 1i$
Aquadag[g]	variable
fullerene soot[h]	variable
smoldering peat[i]	$1.56 - 0.002i$
SAFARI 2000[j]	$1.54 - 0.0094i$
ACE-Asia tarballs[k]	$1.77 - 0.19i$
Lab tarballs[l]	$1.70 - 0.062i$

a) 95 % H_2SO_4 in H_2O (Palmer and Williams, 1975)
b) https://refractiveindex.info
c) Cai et al. 2008
d) Kroschwitz (2004), though crystal form, orientation, and coordinated H_2O could give n from 1.394 to 1.483 (Lide, 2004). These are all at $\lambda = 589$ nm, but IR refractive index should not be far off.
e) Djurišić and Li 1999
f) Moteki et al. 2010
g) Graphite reduced using the mixing rule of Liu and Daum (2008) and effective density from Gysel et al. (2011).
h) Soot reduced using the mixing rule of Liu and Daum (2008) and effective density from Gysel et al. (2011).
i) Sumlin et al. 2018b
j) from Haywood et al. (2003) but k reduced from $0.018i$ assuming $1/\lambda$ dependence of absorption.
k) Asian outflow (Alexander et al., 2008)
l) Lab generated from spruce and locust (Hoffer et al., 2017), extrapolated to 1054 nm and averaged.

200 absorption of particles containing LAC. Following Cai et al. (2008), we use the analysis by Chan (1975) to estimate the change in temperature.

$$\Delta T_{\mathrm{ss}} = I Q_{abs} D_p / 8 k_a \tag{1}$$

where ΔT_{ss} is the steady state temperature difference reflecting the balance between the particle absorbing light energy and losing it to the surrounding air. $I \approx 5.1 \times 10^9 \,\mathrm{Wm}^{-2}$ is the intensity of the beam (≈ 1 kW laser and 0.5 mm beam diameter),
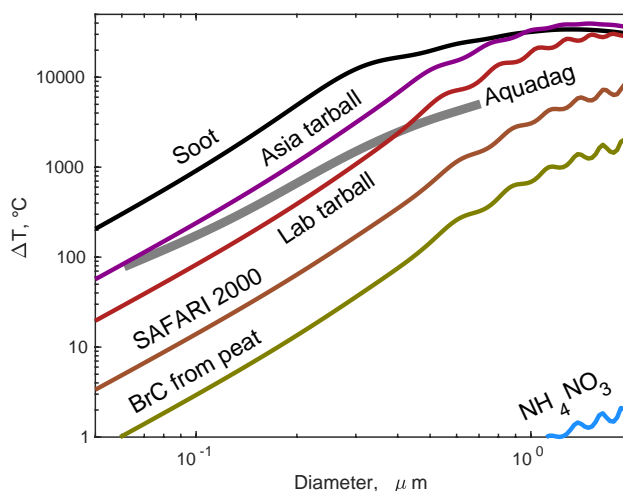
Figure 4. Estimates of particle heating from Eq 1 for several particle composition types. See Table 1 for the refractive indices used.

Q_{abs} is the Mie absorption efficiency, D_p is particle diameter, and $k_a = 0.026\,\mathrm{Wm^{-1}K^{-1}}$ is the thermal conductivity of air. The time constant for heating is

$$\tau = D_p^2 \rho_p c_p / 12 k_a \tag{2}$$

where ρ_p and c_p are the density and heat capacity of the particle. This is approximately 6 µs for 1 µm particles, and shorter for smaller diameters. Time in the beam is much longer, ~ 20 µs, so particles should attain steady state temperatures.

Results from Eq. 1 are shown in Fig. 4. Very weakly absorbing particles such as $\mathrm{NH_4NO_3}$ are not heated significantly, but soot is calculated to achieve up to $34000\,\mathrm{K}$. Particles with the reported refractive index of African biomass burning (SAFARI 2000) reach $4000\,\mathrm{K}$. (But note that few individual particles are likely to have that refractive index–the real aerosol population is likely to have some particles that contain LAC and thus have much higher absorption while particles lacking LAC absorb little.)

Of course, particles never reach these temperatures, as sulfates are gone by 300°C, most organic material evaporates by 400°C, and soot itself boils off at around 4000 K (Schwarz et al., 2006). As particles heat and material leaves, they shrink, absorb less light, and have a lower equilibrium temperature. Since the time constants from Eq. 2 are short compared to time in the beam, it is unlikely that the scattering peak voltage as seen by the UHSAS reflects the initial diameter of an absorbing particle.

It is not entirely clear why the fullerene soot and Aquadag were undersized so dramatically. They ought to remain intact up to ~ 4000 K, a temperature Aquadag is calculated to reach only for particles > 0.5 µm, though that calculation is pretty crude. Among the possibilities are:

The particles heat up and shrink as they boil away. This implies that ultimately any rBC particle would shrink to the same size, where air cooling and laser heating would be in balance at or below the boiling point of rBC. The Mie calculations

225   suggest that would be around 200 nm for pure rBC. Below that, the particles would not heat enough to shrink. That conflicts with Fig. 2, which shows undersizing at 100 nm. Maximum scattering would be a function of the beam profile, the heating rate, and the evaporation rate so larger particles would appear smaller by a difficult-to-predict fraction without the time resolution of an SP2 (Moteki and Kondo, 2007). A related possibility would be that as the particles heat, they collapse into a smaller size. Huang et al. (2007) found that some giant fullerenes collapse by a factor of 10 as they heat

230   but that was at ~2000°C and not true for the C_{60} form of fullerene most common in our test material. One could imagine the carbon actually combusting, thus shrinking the particles, but that apparently does not occur in the SP2, so is unlikely in the UHSAS. After passing through the thermal denuder, Aquadag particles are ~13 % unknown composition Gysel et al. (2011), which must be stable at 450°C, but might evaporate at higher temperatures. That would only produce a 5 % diameter reduction, so is far from a full explanation of the undersizing.

235   **The signal detected is incandescence, not scattering.** Essentially this is the idea that the UHSAS is acting like an SP2, which quantifies rBC by incandescence after heating with a much more powerful IR laser. Because the incandescence is directly proportional to mass of rBC (Moteki and Kondo, 2007), this would yield a slope of 3 in Fig. 2. The actual slope is closer to 4, but a combination of scattering and incandescence could yield that slope. The main drawback to this explanation is that the small particles are unlikely to heat to incandescence. In addition, calculations of the incandescence (assuming

240   blackbody radiation) show that the energy output into the optics is always at least 2 orders of magnitude smaller than the scattering signal. (Only if the APD is much more sensitive to shortwave radiation than to the 1054 nm scattered light would incandescence influence the UHSAS output.)

    Mie scattering is inappropriate for these particles. Aquadag is made of small plates while fullerene soot is a fractal-like arrangement of tiny spheres (Moteki et al., 2009). Complex shapes can increase mobility diameter without increasing

245   scattering. It is surprising that shapes as different as Aquadag and Fullerene would have similar deviations. We tried to take this into account using the effective density, but that may not suffice. It is difficult to imagine that the effect exceeds an order of magnitude, particularly for the small particles in the Rayleigh scattering regime, where Gebhart (1991) shows that even a 5:1 aspect ratio changes scattering by only 27 % and sizing by 4 %.

    Particles experience localized extreme heating. Perhaps the light absorbing moieties are sparsely distributed through the

250   particles and thus heat extremely rapidly and evaporate in small regions of the particles, rather than evenly throughout the particles. That could evaporate material proportional to mass, or even blow particles apart. If the latter were occurring, one would expect very broad resulting size distributions, not the sharp peaks we saw.

Altogether, heating, evaporating, and shrinking is the most plausible reason for this undersizing, even though we cannot explain how the smallest particles get hot enough to evaporate.
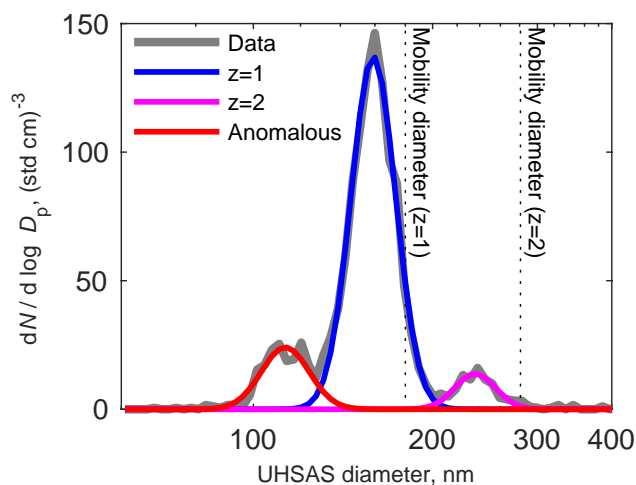
Figure 5. UHSAS size distribution from a DMA selecting 180 nm particles at 1.44 °S, 5 °E at 1919 m altitude on 2018/10/23 around 14:00 UTC. Colored curves are lognormal fits to the gray data line.

3.2 Aerosol sampling during ORACLES

In the 2018 ORACLES deployment, we performed the DMA→UHSAS tests during 15 periods, using particles with (singly charged) mobility diameters between 70 and 180 nm. We usually chose 4 diameters and cycled through them, sampling for 60 seconds each time.

A typical response looks like Figure 5. The biggest peak is plainly the particles selected by the DMA as intended, with a single charge. The width of the fit reflects the kernel function of the DMA (a triangle with curves caused by diffusion), random variation in the UHSAS response, and variations in the scattering property of the particles.

The peak at larger diameter is due to doubly charged particles. A DMA cannot differentiate between a singly charged particle and a doubly charged one with half the mobility diameter. This means we actually get a second, larger particle size. The RDMA could scan up to about 200 nm, depending on altitude; the largest diameter well-defined peak we could get for singly-charged particles was at 180 nm, and corresponding doubly-charged particles were about 280 nm. (The Cunningham slip correction factor was included in the calculation, so mobility is not just the square root of diameter.) Thus we could calibrate only a small fraction of the UHSAS size range, but that included most of the particles in the accumulation mode.

To the left of the singly- and doubly-charged peaks, another mode, containing just a few particles, was present in all of the tests except when the DMA was selecting 80 nm or smaller particles. (That mode may have been present but at diameters below the detection limit of the UHSAS.) This mode appears to be undersized in much the same way as the Aquadag and fullerene particles in the lab calibrations. Thus, we think it most likely that these anomalously undersized particles are the ones containing rBC. This is discussed later, in section 3.4.

It is obvious in Figure 5 that the diameters reported by the UHSAS for both singly and doubly charged particles are considerably smaller than the mobility diameter. This pattern was consistent through all sizes of particles for each test we did. The top
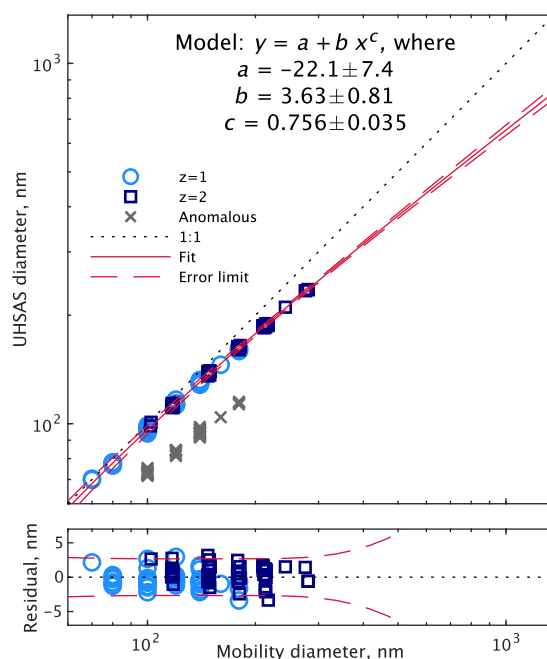
Figure 6. UHSAS reported diameters while sampling size-selected particles from the DMA during flight. Only the singly and doubly charged particles were used in the curve fit; the anomalous particles were excluded. (error bounds are 95 % confidence limits within the fitting range). The bottom plot shows the residuals.

plot in Figure 6 summarizes the results for all of the DMA→UHSAS tests in 2018. The bottom plot shows variability between tests was pretty small, varying no more than $3\,\mathrm{nm}$ from the average. This presumably reflects relatively constant composition through the duration of the 2018 deployment, though we did tend to perform the tests in extended level legs with substantial BB aerosol concentrations, thus perhaps biasing our samples toward constant composition.

We tested a variety of fitting functions with the $z = 1$ and $z = 2$ peaks (omitting the anomalous particles). The simplest function that lacked a strong pattern in the residuals was

$$D_{\mathrm{opt}} = a + b D_{\mathrm{mob}}^{c} \tag{3}$$

where D_{opt} is the optical (UHSAS) diameter, D_{mob} is the mobility diameter from the DMA and a, b, and c are the fitting parameters. Within the RDMA size range, 95 % confidence limits are within $3\,\mathrm{nm}$, but of course the correction is highly speculative beyond that, from $300\,\mathrm{nm}$ to $1\,\mathrm{\mu m}$. In fact it's likely to be completely inappropriate, as particles near $1\,\mathrm{\mu m}$ are usually chemically distinct from smaller particles, typically dust in the FT and sea salt in the MBL.

The undersizing of the $z = 1$ and $z = 2$ particles in Fig. 6 cannot be explained by the refractive index of the BB plume. For spherical, homogeneous, and non-absorbing particles it is straightforward to determine the refractive index required for particles of a known diameter to produce a given scattering signal. The results are shown in Figure 7. The smallest particles
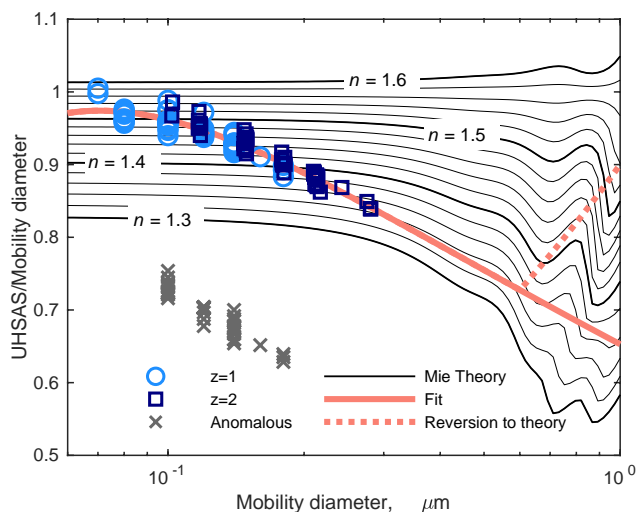
Figure 7. The ratio of apparent to actual diameter measured in the DMA→UHSAS tests superimposed on a contour plot of Mie calculations of refractive index and apparent particle diameter. The labels show real refractive indices; absorption is assumed to be 0. The fit line is from Fig. 6, and the dashed line is an arbitrary modification meant to reflect a transition from BB particles in the accumulation mode to seasalt-like particles at 1 μm. Symbols represent the same data as in Fig. 6.

produce scattering consistent with a refractive index of around 1.52, which is lower than usually reported, but not unreasonable. But the apparent refractive index of larger particles drops rapidly to 1.35, far below any plausible aerosol material. Extrapolating to 0.5 μm gives a refractive index of 1.33, equal to that of water.

The most likely explanation for the undersizing is evaporation of particles as they absorb heat from the UHSAS laser. That is consistent with the exaggerated undersizing for larger particles, which are likely to get hotter, as seen in Eq. 1 and Fig. 4. But what is absorbing IR light from the laser? The only significant absorbing materials commonly present in aerosol particles are rBC, dust, and BrC. Since we think the rBC-containing particles appear as the anomalously small mode, and dust was only occasionally present and is typically on larger particles, BrC is the obvious remaining possibility. We had assumed that that brown carbon would be unlikely to heat this way, as BrC absorption in the IR is weak and is typically considered trivial at long wavelengths (e.g., Yang et al., 2009; Bahadur et al., 2012; Saleh et al., 2013).

IR absorption by BrC has been measured in a few studies. While Li et al. (2020) found negligible absorption for wood tar aerosol above 550 nm, Sumlin et al. (2018b) did find a small amount of absorption, $k = 0.002 \pm 0.005$, for 1047 nm light in smoke from smoldering peat fires in a laboratory. That absorption is only sufficient to heat 300 nm particles by about 25°C (Fig. 4), which would not evaporate a large fraction of organic material. It is not clear what relationship the BrC in either circumstance has to the ORACLES aerosol. During ORACLES, the relatively low absorption Ångström exponent of 1–1.5 (Pistone et al., 2019) indicates that BrC contributions to overall absorption at visible wavelengths were small, but does not exclude some IR absorption.

Tarballs are another possibility. They appear to be ubiquitous in biomass burning plumes (Pósfai et al., 2004), including those in southern Africa (Pósfai et al., 2003). Their incidence increases as plumes age over a few hours, but their size does not, implying that they are primary particles undergoing photochemical aging rather than secondary material condensing (Sedlacek et al., 2018a; Adachi et al., 2019). There is essentially no information available about how they age over the 2 day to 2 week

310   period experienced by the ORACLES plume, but there were some tarballs noted in filter samples taken aboard the plane in 2018 (Michal Segal-Rozenhaimer, personal communication, 2020). There are only a couple of reported complex refractive indices for tarballs at IR wavelengths; they are shown in Table 1. Fig. 4 shows that that tarballs are likely to heat to a few hundred degrees, sufficient to evaporate some of the more volatile species in the aerosol (Ellis and Novakov, 1982). However, reported absorption (k) by tarballs at visible wavelengths spans 2 orders of magnitude Sedlacek et al. (2018a), and the absorption of the

315   Asian outflow tarballs in Alexander et al. (2008) was described as very high and unlikely to be representative of BB tarballs, so our argument that tarballs would heat enough to shrink substantially is not conclusive.

One problem with crediting the UHSAS undersizing to tarballs is that there are only two obvious modes in the DMA→UHSAS tests: moderate undersizing and severe undersizing. But if tarballs are numerous but not dominant, there must be three different types of particles with widely varying absorption properties: tarballs, rBC-containing particles and others. To see only 2 modes,

320   one of the following must be true:

Tarballs behave like other BrC with similar absorption in the IR, heating, and particle shrinkage. This isn't consistent with reported refractive indices for tarballs and BrC, but those are not well known.

Tarballs behave like rBC heating up in the beam, charring, forming rBC, and appearing anomalously small. This has been shown to occur in an SP2 using BrC with relatively high IR absorption (Sedlacek et al., 2018b), so it is plausible in the

325   UHSAS. But that would then get us back to the earlier question of why the vast majority of particles just shrink a little. BrC would be the obvious absorbing species.

Tarballs are rare and BrC absorbs IR . That would be consistent with Pósfai et al. (2003), who saw a high fraction of tarballs in moderately aged plumes, but very few in the regional haze around southern Africa. We do not yet have quantitative information about the actual prevalence of tarballs during ORACLES.

330 **Tarballs dominate** and are responsible for the moderate undersizing mode. This is contrary to Pósfai et al. (2003), who noted that tarballs are highly distinctive in electron microscopy, are usually unmixed with other particle types, and are rare in regional haze. Perhaps after a few days of aging they change appearance or sufficient secondary material condenses onto tarballs to disguise them.

3.3   A simple correction scheme

335 Since the DMA→UHSAS data extend only to 0.28 μm, any extension past that is speculation. When plotting volume distributions, the accumulation mode rarely extended past 0.6 μm. Above that, particles are more likely to be seasalt (in the MBL), dust (in the FT), or sulfate (in a non-dusty FT). In Fig. 7, we show a correction that extends the fit line to 0.6 μm then deviates
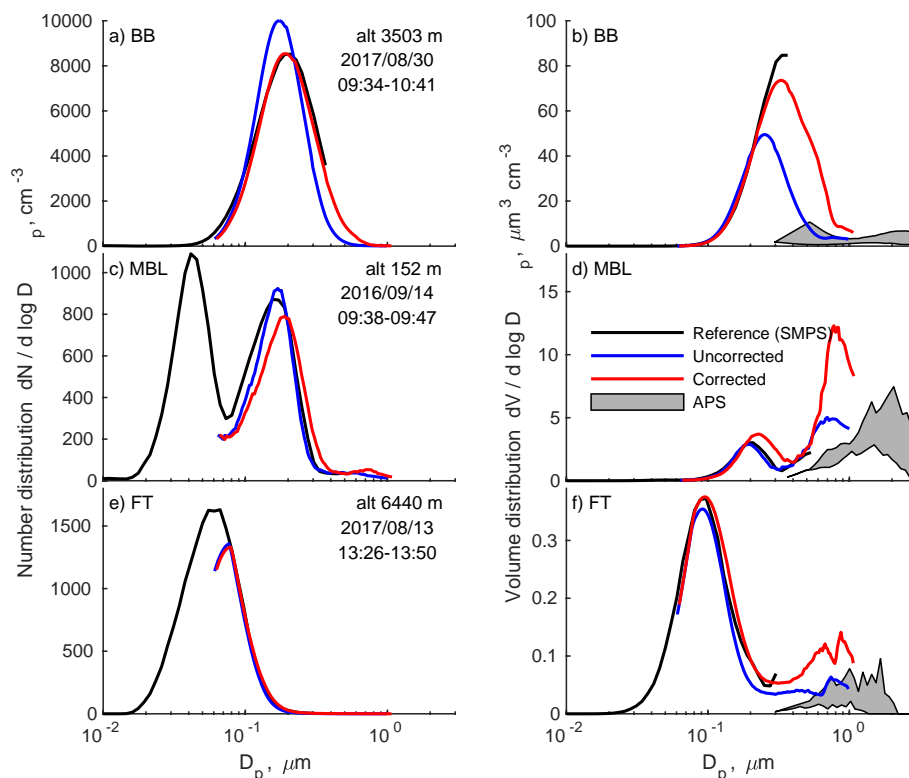
Figure 8. Examples of the proposed correction on samples from the polluted FT (a and b), a clean MBL (c and d), and above the plume in the clean FT (e and f). Plots on the left are number distributions and those on the right are volume distributions, which emphasize the larger particles. Since we don't know the density, the APS data are shown as a shaded region between assumed densities of biomass burning aerosol $(1.2\,\mathrm{g\,cm^{-3}})$, and dust $(3\,\mathrm{g\,cm^{-3}})$ in b) and f), or seasalt $(2.2\,\mathrm{g\,cm^{-3}})$ in d).

along a straight line to the expected diameter ratio for particles with $n = 1.54$, similar to NaCl, a little above (NH4)2SO4, and below silicate minerals. This is just a crude way to suppress really exaggerated oversizing for the non-BB particles larger than

340   the accumulation mode, and should not be considered realistic.

Figure 8 shows the effect of applying that correction to some selected size distributions. Uncorrected and corrected UHSAS distributions are compared with LDMA distributions in the pollution layer, the MBL, and clean FT. Data from 2016 and 2017 were chosen to demonstrate that even though the correction was based on data from 2018, when BB concentrations were lowest, it is appropriate to use the correction for earlier data in the polluted FT. The top left plot, from a period within the BB

345   plume, shows that the correction makes the UHSAS agree quite well with the LDMA. The effect on the volume distribution, top right, is dramatic, as the uncorrected data are far below the LDMA distribution. The correction is plainly inappropriate in a clean MBL sample, where the correction overestimates peak particle diameter and accumulation mode volume and is far too high near 1 µm compared with the APS. (Without the transition to NaCl refractive index, it is far worse.) In the clean

troposphere, the number peak is at sufficiently small diameters that the correction makes very little difference, so it doesn't
350   matter much whether the correction is used.

When applied to accumulation mode particles in the FT plume, the overall effect of the correction is to increase the median diameter by 13 to 18 nm. In 2018, the least polluted year, the median diameter rose from 143 to 156 nm, while for 2017, median diameter went from 163 to 181 nm with the correction applied.

The danger of extrapolating the correction to diameters above 600 nm even with the arbitrary reversion to $n = 1.54$ is
355   obvious in the volume distributions shown on the right side of Figure 8. Comparisons between UHSAS and APS are not straightforward and are highly sensitive to assumed density, but it is clear that in each of these cases the corrected UHSAS is an order of magnitude too high near 1 μm.

In contrast, scattering emphasizes the large particles less, so the correction fares considerably better, as can be seen in Figure 9, where scattering calculated from the UHSAS distributions is compared to the TSI nephelometer. The correction
360   increases calculated scattering by a factor of about 2.3 in each year, improving agreement considerably. The nephelometers sense scattering between 7° and 170° (Anderson et al., 1996) so the UHSAS scattering calculation was performed over that range of angles rather than the full 0° to 180° range. This is a more direct comparison than correcting the nephelometer data for truncation errors. Total rather than sub-μm data are shown because scattering was almost always dominated by the accumulation mode, so the total and submicron nephelometers usually agreed well and over the course of the project we had
365   more data from the total nephelometer. This means the comparison is worse at low altitude, when coarse seasalt particles can account for considerable scattering. This effect is clear, as the dark blue low altitude points are concentrated at the bottom of the data clouds.

While encouraging, the scattering calculation is subject to some major uncertainties, so may have compensating errors:

-     Since this nephelometer did not have an impactor removing sub-μm particles, when dust or seasalt were present they
370   increase scattering but are not sensed by the UHSAS. *UHSAS small underestimate.*

-     The same correction is applied to the anomalously undersized particles, which are likely to be 10–35 % of the accumulation mode, as shown below. *UHSAS underestimate.*

-     It is not clear what refractive index to use here. We used the PSL refractive index, but the real aerosol presumably has a lower real part and a higher imaginary component. *UHSAS overestimate?*

375   -   The nephelometer RH was uncontrolled, while in 2017 and 2018 the UHSAS sample was diluted with desiccated air. At high altitudes heating to cabin temperature ensured low RH in all instruments, but nephelometer RH in the MBL occasionally exceeded 50 %. *UHSAS underestimate at low altitudes*

3.4   The anomalous particles

The particles sized anomalously small in Figs. 5 and 6 are a bit of a mystery. The obvious explanation is that they are rBC
380   particles and behave the same way as the lab tests of fullerene soot and Aquadag (Fig. 2). But the SP2 data indicate that rBC
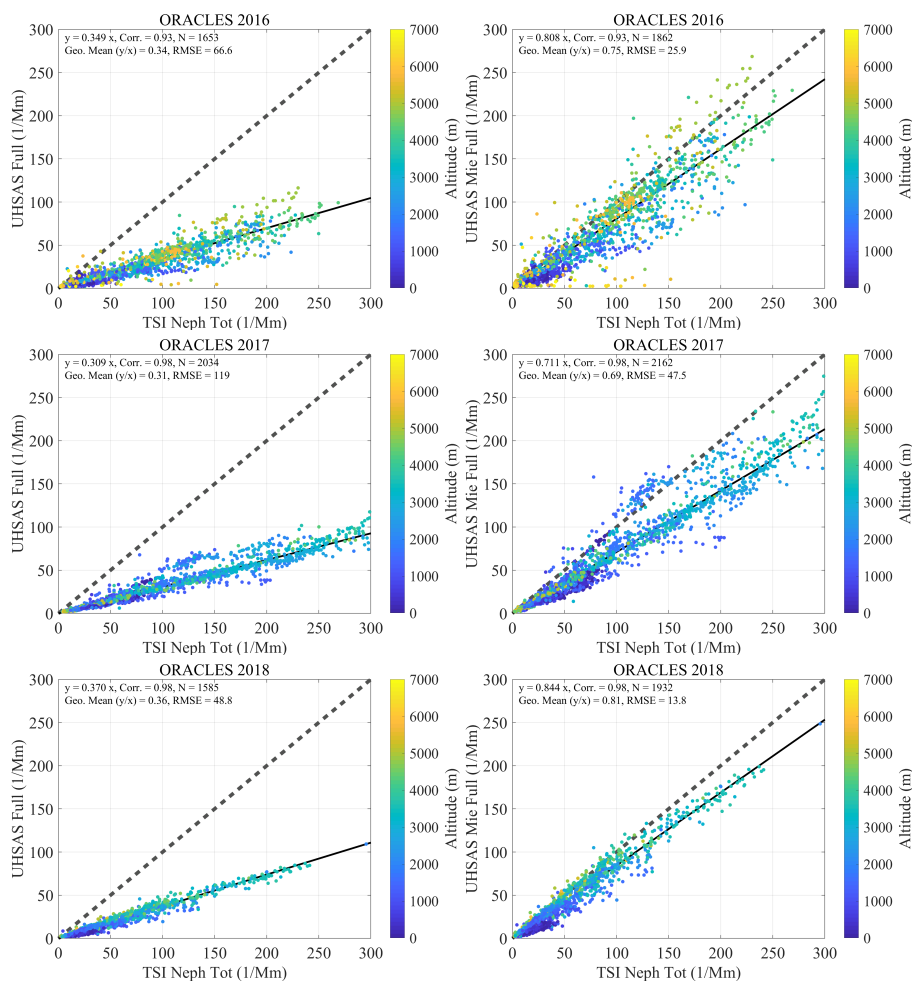
Figure 9. Effect of the proposed correction on scattering closure calculations at 550 nm. Plots on the left use uncorrected UHSAS distributions from each year of ORACLES while those on the right use the corrected distributions. Nephelometer data are uncorrected for truncation error; instead the scattering from the UHSAS size distribution is calculated over the 7 to 170 degree sensing range of the nephelometer. The refractive index used in the calculation is 1.588, that of the PSL calibration spheres at visible wavelengths. The 2017 data include a few points above $300~\mathrm{Mm}^{-1}$ that are not shown.

was typically coated with a thick layer of volatile material. In one sense, that makes extensive shrinkage easier to understand– temperatures of 400°C are sufficient to remove much of the coating, rather than the 4000°C required to evaporate graphite. But in that case, these shrunken cores ought to be dramatically undersized, as the Aquadag and fullerene soot were. Instead, they look about the same.

385   It is possible that at least some of these anomalously small particles contain no BC at all, but absorb enough IR that organic materials char and become rBC which then absorbs more IR, heating the particle enough to shrink it a lot. This seems particu-
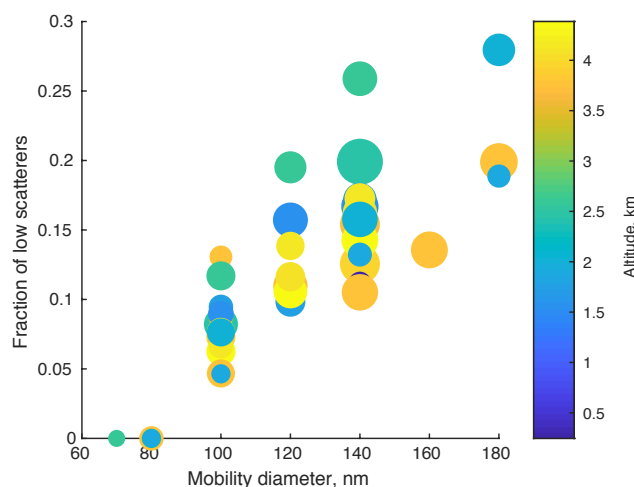
Figure 10. Ratio of anomalous to singly charged particles vs. mobility diameter. It is apparent that these anomalously low scattering particles are more common at larger diameters and are somewhat less common high in the plume. Circle sizes are proportional to concentration at that diameter; there is no obvious pattern. The UHSAS lower size detection limit precludes detecting these particles below 70 nm.

larly likely for tarballs, as mentioned above. Such charring behavior has been identified in the lab by Sedlacek et al. (2018b), who found that nigrosin particles appeared to an SP2 as rBC with approximately 40 % of the mass of the original particles. That works out to about 70 % of the original diameter, roughly consistent with our anomalous particles (Fig. 7). There were

390 also indications of this in ORACLES when we made a short-lived attempt in 2017 to explore whether volatile coatings on particles enhanced absorption. We planned to test this by passing particles through a 400°C denuder on the way to one of the two PSAPS (3-wavelength Particle Soot Absorption Photometers) on board, anticipating that evaporating some of the coating would reduce absorption. However, the heat treatment increased absorption rather than decreasing it, indicating that charring was taking place.

395 It would be useful to send size-selected particles to the SP2 and UHSAS simultaneously in future experiments; that would allow us to directly measure the fraction of particles at each size that contain rBC and how much rBC mass was contained in those particles.

The fraction of these anomalous particles is a strong function of particle size (Fig. 10). Below 100 nm, they are either absent or too small to see, but at 180 nm they are over 20 % of the $z = 1$ peak. There were undoubtedly undersized doubly charged

400 particles, but they are hidden by the singly-charged particle peaks. This may mean the number of singly-charged particles is an overestimate and hence the fraction of low scatterers is larger than evident in Fig. 10.

There is also general dependence on altitude, with particles from >3.5 km tending to have fewer anomalous particles than those from lower altitude, though that pattern is a bit noisy. It may be related to other chemical differences we saw with altitude reflecting plume aging Redemann et al. (2020), but that will require further exploration.
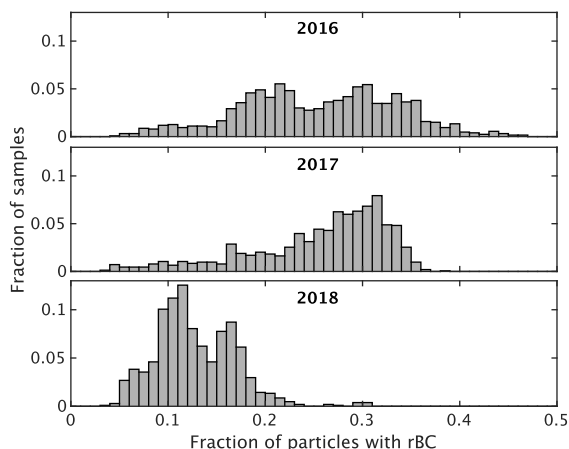
Figure 11. The fraction of particles that contained significant rBC in each ORACLES deployment, determined as the ratio of incandescing particles in the SP2 to CN concentration while in the BB plume (altitude > 1500m and rBC concentrations $>50\,\mathrm{cm}^{-3}$.)

While we cannot prove that the anomalous particles are the ones containing rBC, it is roughly consistent with the over-all fraction of rBC-bearing particles shown in Fig. 11. The drastically undersized particles average only 15 to 20 % in the DMA→UHSAS tests, but that may be an underestimate, as mentioned above. In addition, the accumulation mode median particle diameter was roughly 170 nm, averaged over all three years, so the data shown in Fig. 10 only cover half of the size distribution and the relatively high points at the right are the most representative.

Fig 11 also appears to shed some light on the patterns seen in the scattering closure calculations (Fig. 9). Since the anomalous particles are sized roughly 30 % small, scattering calculated from them is less than half of the real value. In 2018, that affected 10–17 % of the particles, and the calculated scattering was ∼20 % low. In 2017, by contrast, roughly 30 % of the particles had rBC and calculated scattering was 30 % low. 2016 was in between.

4   Conclusions

While for non-absorbing particles, the characteristics of the UHSAS greatly reduce uncertainties due to Mie wiggles, absorbing material complicates the situation, apparently because the very intense IR laser heats the particles. During the ORACLES project over the southeast Atlantic Ocean, the NASA P-3B was often in a fairly uniform biomass burning plume for periods exceeding 30 minutes, allowing time to explore the details of the UHSAS response by selecting single particle sizes with a DMA and passing them to the UHSAS. Two modes of responses appeared. Most particles were moderately undersized, apparently due to heating of brown carbon. A fraction were dramatically (∼30 %) undersized, presumably because they contained more absorbing rBC. It would be interesting in future projects to send size-selected particles to the SP2 as well, so the size-dependent fraction of particles containing rBC could be determined.

Mie calculations using the geometry of the UHSAS showed that the refractive index of the particles was an insufficient explanation of the undersizing. An empirical correction equation $D_{\mathrm{opt}} = a + bD_{\mathrm{mob}}^c$ dramatically improves agreement with DMA distributions between 100 and 500 nm and with scattering closure calculations. This raises median particle diameters between 13 and 17 nm in project average size distributions. The correction is only valid in polluted instances; clean marine boundary layer and free troposphere aerosols behaved more like the calibration spheres. We were unable to directly test the correction between 500 and 1000 nm, though APS data appear to show that the correction fails at the largest diameters, which is no surprise as the composition of those particles are likely to be dust or sea salt, with quite different refractive indices.

Our findings differ a bit from Yokelson et al. (2011), who contend that absorbing particles are essentially invisible to the UHSAS. Instead, the particles are drastically undersized. That leads to complications interpreting size distributions in a rBC-rich plume, when up to 35 % of the particles are likely to suffer this mis-measurement (Fig. 11). Therefore, the relatively slow DMA measurements (one sample every 85 s) must be regarded as the most reliable diameter measurement, with the UHSAS providing rapid response and filling the gap between DMA and APS measurements.

In ORACLES we were fortunate to have numerous redundant sizing instruments available to identify the UHSAS issues. Combustion efficiency for the African fires was quite high, which is typically associated with a high ratio of rBC to organics, so the severely undersized fraction of particles was clearly evident. Such behavior could be important to resolve for other studies using the UHSAS that focus on combustion-derived aerosol and the radiative properties of the size distribution or its relationship to CCN. Moreover, the IR absorption of BrC is little studied, poorly known, and may vary with fuel type, combustion conditions, and aging during transport, so the behavior in the UHSAS may not be the same.

Code and data availability. All data from ORACLES are available at the following DOIs:

2018 P3 data ORACLES Science Team: Suite of Aerosol, Cloud, and Related Data Acquired Aboard P3 During ORACLES 2018, Version 2, NASA Ames Earth Science Project Office, 2020, Accessible at doi://10.5067/Suborbital/ORACLES/P3/2018_V2

2017 P3 data ORACLES Science Team: Suite of Aerosol, Cloud, and Related Data Acquired Aboard P3 During ORACLES 2017, Version 2, NASA Ames Earth Science Project Office, 2020, Accessible at doi://10.5067/Suborbital/ORACLES/P3/2017_V2

2016 P3 data ORACLES Science Team: Suite of Aerosol, Cloud, and Related Data Acquired Aboard P3 During ORACLES 2016, Version 2, NASA Ames Earth Science Project Office, 2020, Accessible at doi://10.5067/Suborbital/ORACLES/P3/2016_V2

2016 ER2 data ORACLES Science Team: Suite of Aerosol, Cloud, and Related Data Acquired Aboard ER2 During ORACLES 2016, Version 2, NASA Ames Earth Science Project Office, 2020, Accessible at doi://10.5067/Suborbital/ORACLES/ER2/2016_V2

Processing code is available as well. The Mie calculation code in Matlab is available on request.

Appendix A: Mie scattering calculations

Light scattering by any particle can be represented by 4 amplitude functions, S_1, S_2, S_3, and S_4, which are complex functions dependent on the angles of the incident beam and the scattered light. For homogeneous spheres, only S_1 and S_2 are nonzero

(van de Hulst, 1957) and are functions of the Mie parameter $\pi D_p/\lambda$ and the refractive index $m = n - ik$. D_p is particle

455   diameter, λ is wavelength, n is the real part of the refractive index, and k is the complex, absorbing part of the refractive index.

     The intensity of light scattered from a single homogeneous spherical particle is proportional to the square of the magnitude of the amplitude functions:

$$I_\perp = \frac{\lambda^2}{4\pi^2 r^2} \left|S_1(\theta)\right|^2 I_0 \tag{A1}$$

for perpendicular polarization and

460
$$I_\parallel = \frac{\lambda^2}{4\pi^2 r^2} \left|S_2(\theta)\right|^2 I_0 \tag{A2}$$

for parallel polarization, where θ is the scattering angle, λ is the wavelength of light, r is the distance from the particle, and I_0 is the intensity of the illuminating beam as power per unit area.

     The UHSAS laser is reflected within the cavity, so the beam is going both ways, doubling the intensity:

$$I_\perp = \frac{\lambda^2}{4\pi^2 r^2} I_0 \left[\left|S_1(\theta)\right|^2 + \left|S_1(\pi - \theta)\right|^2 \right] \tag{A3}$$

465   and

$$I_\parallel = \frac{\lambda^2}{4\pi^2 r^2} I_0 \left[\left|S_2(\theta)\right|^2 + \left|S_2(\pi - \theta)\right|^2 \right] \tag{A4}$$

     Combining Eqs. A3 and A4 using the angle ϕ from parallel polarization and substituting $\mathbb{S}_1(\theta)$ and $\mathbb{S}_2(\theta)$ for the quantities in the square brackets gives the total intensity as a function of position:

$$I = \frac{\lambda^2}{4\pi^2 r^2} I_0 \left[\mathbb{S}_1(\theta) \sin^2 \phi + \mathbb{S}_2(\theta) \cos^2 \phi \right] \tag{A5}$$

470   Power into the detector is the integral of the intensity over the collection area of the optics:

$$P = \frac{\lambda^2}{4\pi^2} I_0 \int_A \frac{1}{r^2} \left[\mathbb{S}_1(\theta) \sin^2 \phi + \mathbb{S}_2(\theta) \cos^2 \phi \right] dA \tag{A6}$$

Realizing that $dA = r^2 \sin\theta \, d\phi \, d\theta$ and multiplying by a constant C_{opt} that includes the efficiency of the mirrors, the sensitivity of the detector, and the amplification of the output circuit gives the output voltage of the detector as

$$V = C_{\text{opt}} \frac{\lambda^2}{4\pi^2} I_0 \iint_{\theta \, \phi} \left[\mathbb{S}_1(\theta) \sin^2 \phi + \mathbb{S}_2(\theta) \cos^2 \phi \right] \sin\theta \, d\phi \, d\theta \tag{A7}$$

475   It is assumed in Eqs. A3 and A4 that the UHSAS is not an active cavity device–beams going each direction are not coherent; they do not interfere with each other and no standing wave pattern is present. If it were, scattering from individual particles

would depend on precisely where the particle meets the beam and on average would require summing the scattering amplitudes before calculating intensity (Garvey and Pinnick, 1983). This just means redefining $\mathbb{S}_1$ and $\mathbb{S}_2$:

$$\mathbb{S}_1(\theta) = |S_1(\theta) + S_1(\pi - \theta)|^2 \tag{A8}$$

480 and

$$\mathbb{S}_2(\theta) = |S_2(\theta) + S_2(\pi - \theta)|^2 \tag{A9}$$

While the DMT PCASP (Passive Cavity Aerosol Spectrometer Probe) has a vibrating mirror to suppress these standing waves (Rosenberg et al., 2012), the UHSAS does not actively avoid coherence. The manufacturer reports that it is "not a single-mode laser and the coherence time is quite small" (personal communication with DMT, 2017). This is unlike the TSI 3340 OPC,

485 which has detection optics very similar to the UHSAS but an active-cavity HeNe laser ($633\mathrm{nm}$) where the manual mentions a standing wave mode.

The implementation is straightforward and fairly primitive: given the refractive index m, wavelength λ, and a vector of particle diameters, S_1 and S_2 are calculated for $\theta = 0$ to π radians (default resolution is $0.5°$). Then the quantities in the integral of Eq. A7 are calculated at each θ and ϕ, and points within the collection region of the optics are summed.

490 The code used is quite general; it is designed to calculate scattering into arbitrarily oriented annular regions so essentially any single-wavelength OPC can be represented. There are options to define $\mathbb{S}_1$ and $\mathbb{S}_2$ as in Eqs. A8 and A9 for exploring the impact of active cavities or simply as $\mathbb{S}_1(\theta) = |S_1(\theta)|^2$ and $\mathbb{S}_2(\theta) = |S_2(\theta)|^2$ for instruments without an intracavity laser such as the Grimm and MetONE OPCs and for forward scattering instruments like the Forward Scattering Spectrometer Probe (FSSP) and Cloud Droplet Probe (CDP).

495 *Author contributions.* N.S. performed the lab tests and operated the in-flight instrumentation. S.F. helped design the experiment, participated in lab work and flight work, did much of the data processing and extended analysis, submitted the data to the archive, and helped with paper writing. S.H. operated the equipment, helped design the experiment, did many of the calculations, and wrote the paper. A.S. operated the SP2 and processed the data and contributed editorial content. A.D. also operated in-flight instrumentation and provided help in the lab.

Competing interests. The authors declare that they have no conflict of interest.

500 *Acknowledgements.* We are grateful to the entire NASA Wallops aircraft team: pilots, air crew, techs and engineers who worked with the P-3B. In addition NASA's ESPO group provided extremely valuable logistical support. We'd also like to thank the whole ORACLES team for uniting to make such a pleasant and productive project. Funding was from NASA grant NNX15AG01G.

References

Adachi, K., Sedlacek III, A. J., Kleinman, L., Springston, S. R., Wang, J., Chand, D., Hubbe, J. M., Shilling, J. E., Onasch, T. B., Kinase, T., Sakata, K., Takahashi, Y., and Buseck, P. R.: Spherical tarball particles form through rapid chemical and physical changes of organic matter in biomass-burning smoke., P. Natl. Acad. Sci. USA, 116, 19 336–19 341, https://doi.org/10.1073/pnas.1900129116, 2019.

Albrecht, B. A.: Aerosols, cloud microphysics, and fractional cloudiness, Science, 245, 1227–1230, https://doi.org/10.1126/science.245.4923.1227, 1989.

Alexander, D. T. L., Crozier, P. A., and Anderson, J. R.: Brown Carbon Spheres in East Asian Outflow and Their Optical Properties, Science, 321, 833–836, https://doi.org/10.1126/science.1155296, 2008.

Ames, R. B., Hand, J. L., Kreidenweis, S. M., Day, D. E., and Malm, W. C.: Optical Measurements of Aerosol Size Distributions in Great Smoky Mountains National Park: Dry Aerosol Characterization, J. Air Waste Manage., 50, 665–676, https://doi.org/10.1080/10473289.2000.10464128, 2000.

Anderson, T., Covert, D., Marshall, S., Laucks, M., Charlson, R., Waggoner, A., Ogren, J., Caldow, R., Holm, R., Quant, F., Sem, G., Wiedensohler, A., Ahlquist, N., and Bates, T.: Performance Characteristics of a High-Sensitivity, Three-Wavelength, Total Scatter/Backscatter Nephelometer, J. Atmos Ocean Tech, 13, 967–986, https://doi.org/10.1175/1520-0426(1996)013<0967:PCOAHS>2.0.CO;2, 1996.

Andreae, M. O. and Gelencser, A.: Black carbon or brown carbon? The nature of light-absorbing carbonaceous aerosols, Atmos. Chem. Phys., 6, 3131–3148, https://doi.org/10.5194/acp-6-3131-2006, 2006.

Bahadur, R., Praveen, P. S., Xu, Y., and Ramanathan, V.: Solar absorption by elemental and brown carbon determined from spectral observations, P. Natl. Acad. Sci. USA, 109, 17 366–17 371, https://doi.org/10.1073/pnas.1205910109, 2012.

Baron, P. A. and Willeke, K.: Aerosol Measurement: Principles, Techniques, and Applications, chap. Aerosol Fundamentals, Van Nostrand Reinhold, New York, 1993.

Bohren, C. F. and Huffman, D. R.: Absorption and Scattering of Light by Small Particles, John Wiley & Sons, 1983.

Bond, T. C. and Bergstrom, R. W.: Light Absorption by Carbonaceous Particles: An Investigative Review, Aerosol Sci. Tech., 40, 27–67, https://doi.org/10.1080/02786820500421521, 2006.

Boucher, O., Randall, D., Artaxo, P., Bretherton, C., Feingold, G., Forster, P., Kerminen, V.-M., Kondo, Y., Liao, H., Lohmann, U., Rasch, P., Satheesh, S., Sherwood, S., Stevens, B., and Zhang, X.: Climate Change 2013: The Physical Science Basis. Contribution of Working Group I to the Fifth Assessment Report of the Intergovernmental Panel on Climate Change, chap. Clouds and Aerosols, Cambridge University Press, Cambridge, United Kingdom and New York, NY, USA, 2013.

Burnett, R., Chen, H., Szyszkowicz, M., Fann, N., Hubbell, B., Pope, C. A., Apte, J. S., Brauer, M., Cohen, A., Weichenthal, S., Coggins, J., Di, Q., Brunekreef, B., Frostad, J., Lim, S. S., Kan, H., Walker, K. D., Thurston, G. D., Hayes, R. B., Lim, C. C., Turner, M. C., Jerrett, M., Krewski, D., Gapstur, S. M., Diver, W. R., Ostro, B., Goldberg, D., Crouse, D. L., Martin, R. V., Peters, P., Pinault, L., Tjepkema, M., van Donkelaar, A., Villeneuve, P. J., Miller, A. B., Yin, P., Zhou, M., Wang, L., Janssen, N. A. H., Marra, M., Atkinson, R. W., Tsang, H., Quoc Thach, T., Cannon, J. B., Allen, R. T., Hart, J. E., Laden, F., Cesaroni, G., Forastiere, F., Weinmayr, G., Jaensch, A., Nagel, G., Concin, H., and Spadaro, J. V.: Global estimates of mortality associated with long-term exposure to outdoor fine particulate matter, P. Natl. Acad. Sci. USA, 115, 9592–9597, https://doi.org/10.1073/pnas.1803222115, 2018.

Cai, Y., Montague, D. C., Mooiweer-Bryan, W., and Deshler, T.: Performance characteristics of the ultra high sensitivity aerosol spectrometer for particles between 55 and 800nm: Laboratory and field studies, J. Aerosol Sci., 39, 759–769, https://doi.org/10.1016/j.jaerosci.2008.04.007, 2008.

540   Chadwick, O. A., Derry, L. A., Vitousek, P. M., Huebert, B. J., and Hedin, L. O.: Changing sources of nutrients during four million years of ecosystem development, Nature, 397, 491–497, https://doi.org/10.1038/17276, 1999.

Chan, C. H.: Effective absorption for thermal blooming due to aerosols, Appl. Phys. Lett., 26, 628–630, https://doi.org/10.1063/1.88003, 1975.

Chen, B., Cheng, Y., and Yeh, H.: Experimental responses of two optical particle counters, J. Aerosol Sci., 15, 457 – 464,
545   https://doi.org/10.1016/0021-8502(84)90041-7, 1984.

Clarke, A. D.: A Thermo-optic Technique for in situ Analysis of Size-resolved Aerosol Physicochemistry, Atmos Environ. A–Gen., 25A, 635–644, https://doi.org/10.1016/0960-1686(91)90061-B, 1991.

Clarke, A. D., Varner, J. L., Eisele, F., Mauldin, R. L., Tanner, D., and Litchy, M.: Particle production in the remote marine atmosphere: Cloud outflow and subsidence during ACE 1, J. Geophys. Res.–Atmos., 103, 16 397–16 409, https://doi.org/10.1029/97JD02987, 1998.

550   Clarke, A. D., Shinozuka, Y., Kapustin, V. N., Howell, S., Huebert, B., Doherty, S., Anderson, T., Covert, D., Anderson, J., Hua, X., Moore, K. G., McNaughton, C., Carmichael, G., and Weber, R.: Size distributions and mixtures of dust and black carbon aerosol in Asian outflow: Physiochemistry and optical properties, J. Geophys. Res.–Atmos., 109, D15S09, https://doi.org/10.1029/2003JD004378, 2004.

Djurišić, A. B. and Li, E. H.: Optical properties of graphite, J. Appl. Phys., 85, 7404–7410, https://doi.org/10.1063/1.369370, 1999.

Droplet Measurement Technologies: Ultra High Sensitivity Aerosol Spectrometer (UHSAS) Operator Manual, 2400
555   Trade Center Ave, Longmont CO, USA, DOC-0210 Rev E-4 edn., https://www.dropletmeasurement.com/manual/operator-manual-ultra-high-sensitivity-aerosol-spectrometer-uhsas/, 2013.

Ellis, E. C. and Novakov, T.: Application of Thermal Analysis to the Characterization of Organic Aerosol Particles, in: Atmospheric Pollution 1982, edited by Benarie, M. M., vol. 20 of *Studies in Environmental Science*, pp. 227 – 238, Elsevier, https://doi.org/doi.org/10.1016/S0166-1116(08)71009-4, 1982.

560   Garvey, D. M. and Pinnick, R. G.: Response Characteristics of the Particle Measuring Systems Active Scattering Aerosol Spectrometer Probe (ASASP–X), Aerosol Sci. Tech., 2, 477–488, https://doi.org/10.1080/02786828308958651, 1983.

Gebhart, J.: Response of Single-Particle Optical Counters to Particles of irregular shape, Part. Part. Syst. Char., 8, 40–47, https://doi.org/10.1002/ppsc.19910080109, 1991.

Gebhart, J.: Aerosol Measurement: Principles, Techniques, and Applications, chap. Optical Direct-Reading Techniques: Light Intensity
565   Systems, Van Nostrand Reinhold, New York, 1993.

Gysel, M., Laborde, M., Olfert, J. S., Subramanian, R., and Gröhn, A. J.: Effective density of Aquadag and fullerene soot black carbon reference materials used for SP2 calibration, Atmos. Meas. Tech., 4, 2851–2858, https://doi.org/10.5194/amt-4-2851-2011, 2011.

Hand, J. L. and Kreidenweis, S. M.: A New Method for Retrieving Particle Refractive Index and Effective Density from Aerosol Size Distribution Data, Aerosol Sci. Tech., 36, 1012–1026, https://doi.org/10.1080/02786820290092276, 2002.

570   Haywood, J. M., Osborne, S. R., Francis, P. N., Keil, A., Formenti, P., Andreae, M. O., and Kaye, P. H.: The mean physical and optical properties of regional haze dominated by biomass burning aerosol measured from the C-130 aircraft during SAFARI 2000, J. Geophys. Res.–Atmos., 108, https://doi.org/10.1029/2002JD002226, 2003.

Hoffer, A., Tóth, Á., Pósfai, M., Chung, C. E., and Gelencsér, A.: Brown carbon absorption in the red and near-infrared spectral region, Atmos. Meas. Tech., 10, 2353–2359, https://doi.org/10.5194/amt-10-2353-2017, 2017.

575   Huang, J. Y., Ding, F., Jiao, K., and Yakobson, B. I.: Real Time Microscopy, Kinetics, and Mechanism of Giant Fullerene Evaporation, Phys. Rev. Lett., 99, https://doi.org/10.1103/physrevlett.99.175503, 2007.

Kroschwitz, J. I., ed.: Kirk-Othmer Encyclopedia of Chemical Technology., vol. 22, J. Wiley, Hoboken, N.J., 2004.

Li, C., He, Q., Hettiyadura, A. P. S., Käfer, U., Shmul, G., Meidan, D., Zimmermann, R., Brown, S. S., George, C., Laskin, A., and Rudich, Y.: Formation of Secondary Brown Carbon in Biomass Burning Aerosol Proxies through NO3 Radical Reactions, Environ. Sci. Technol., 54, 1395–1405, https://doi.org/10.1021/acs.est.9b05641, pMID: 31730747, 2020.

Lide, D. R., ed.: CRC Handbook of Chemistry and Physics, CRC Press, New York, 85th edn., 2004.

Liu, B., Szymanski, W., and Ahn, K.-H.: On Aerosol Size Distribution Measurement by Laser and White Light Optical Particle Counters, J. Environ. Sci., 28, 19–24, https://doi.org/10.17764/jiet.1.28.3.k873425806586048, 1985.

Liu, Y. and Daum, P. H.: Relationship of refractive index to mass density and self-consistency of mixing rules for multicomponent mixtures like ambient aerosols, J. Aerosol Sci., 39, 974 – 986, https://doi.org/10.1016/j.jaerosci.2008.06.006, 2008.

McNaughton, C. S., Clarke, A. D., Howell, S. G., Pinkerton, M., Anderson, B., Thornhill, L., Winstead, E., Hudgins, C., Dibb, J. E., Scheuer, E., and Maring, H.: Results from the DC-8 inlet characterization experiment (DICE): Airborne versus surface sampling of mineral dust and sea salt aerosols, Aerosol Sci. Tech., 41, 136–159, https://doi.org/10.1080/02786820601118406, 2007.

McNaughton, C. S., Clarke, A. D., Kapustin, V., Shinozuka, Y., Howell, S. G., Anderson, B. E., Winstead, E., Dibb, J., Scheuer, E., Cohen, R. C., Wooldridge, P., Perring, A., Huey, L. G., Kim, S., Jimenez, J. L., Dunlea, E. J., DeCarlo, P. F., Wennberg, P. O., Crounse, J. D., Weinheimer, A. J., and Flocke, F.: Observations of heterogeneous reactions between Asian pollution and mineral dust over the Eastern North Pacific during INTEX-B, Atmos. Chem. Phys., 9, 8283–8308, https://doi.org/10.5194/acp-9-8283-2009, 2009.

Mie, G.: Beiträge zur Optik trüber Medien, speziell kolloidaler Metallösungen (Contributions to the Optics of Turbid Media, Particularly of Colloidal Metal Solutions), Ann. Phys., 330, 377–445, https://doi.org/10.1002/andp.19083300302, 1908.

Moteki, N. and Kondo, Y.: Effects of Mixing State on Black Carbon Measurements by Laser-Induced Incandescence, Aerosol Sci. Tech., 41, 398–417, https://doi.org/10.1080/02786820701199728, 2007.

Moteki, N., Kondo, Y., Takegawa, N., and Nakamura, S.-I.: Directional dependence of thermal emission from nonspherical carbon particles, J. Aerosol Sci., 40, 790–801, https://doi.org/10.1016/j.jaerosci.2009.05.003, 2009.

Moteki, N., Kondo, Y., and ichi Nakamura, S.: Method to measure refractive indices of small nonspherical particles: Application to black carbon particles, J. Aerosol Sci., 41, 513 – 521, https://doi.org/10.1016/j.jaerosci.2010.02.013, 2010.

Palmer, K. F. and Williams, D.: Optical constants of sulfuric acid; application to the clouds of Venus?, Appl. Optics, 14, 208–219, https://doi.org/10.1364/AO.14.000208, 1975.

Pistone, K., Redemann, J., Doherty, S., Zuidema, P., Burton, S., Cairns, B., Cochrane, S., Ferrare, R., Flynn, C., Freitag, S., Howell, S. G., Kacenelenbogen, M., LeBlanc, S., Liu, X., Schmidt, K. S., Sedlacek III, A. J., Segal-Rozenhaimer, M., Shinozuka, Y., Stamnes, S., van Diedenhoven, B., Van Harten, G., and Xu, F.: Intercomparison of biomass burning aerosol optical properties from in situ and remote-sensing instruments in ORACLES-2016, Atmos. Chem. Phys., 19, 9181–9208, https://doi.org/10.5194/acp-19-9181-2019, 2019.

Pósfai, M., Simonics, R., Li, J., Hobbs, P. V., and Buseck, P. R.: Individual aerosol particles from biomass burning in southern Africa: 1. Compositions and size distributions of carbonaceous particles, J. Geophys. Res.–Atmos., 108, https://doi.org/10.1029/2002JD002291, 2003.

Pósfai, M., Gelencsér, A., Simonics, R., Arató, K., Li, J., Hobbs, P. V., and Buseck, P. R.: Atmospheric tar balls: Particles from biomass and biofuel burning, J. Geophys. Res.–Atmos., 109, https://doi.org/10.1029/2003JD004169, 2004.

Redemann, J., Wood, R., Zuidema, P., Doherty, S. J., Luna, B., LeBlanc, S. E., Diamond, M. S., Shinozuka, Y., Chang, I. Y., Ueyama, R., Pfister, L., Ryoo, J., Dobracki, A. N., da Silva, A. M., Longo, K. M., Kacenelenbogen, M. S., Flynn, C. J., Pistone, K., Knox, N. M., Piketh, S. J., Haywood, J. M., Formenti, P., Mallet, M., Stier, P., Ackerman, A. S., Bauer, S. E., Fridlind, A. M., Carmichael, G. R., Saide, P. E., Ferrada, G. A., Howell, S. G., Freitag, S., Cairns, B., Holben, B. N., Knobelspiesse, K. D., Tanelli, S., L'Ecuyer, T. S.,

Dzambo, A. M., Sy, O. O., McFarquhar, G. M., Poellot, M. R., Gupta, S., O'Brien, J. R., Nenes, A., Kacarab, M. E., Wong, J. P. S., Small-Griswold, J. D., Thornhill, K. L., Noone, D., Podolske, J. R., Schmidt, K. S., Pilewskie, P., Chen, H., Cochrane, S. P., Sedlacek, A. J., Lang, T. J., Stith, E., Segal-Rozenhaimer, M., Ferrare, R. A., Burton, S. P., Hostetler, C. A., Diner, D. J., Platnick, S. E., Myers, J. S., Meyer, K. G., Spangenberg, D. A., Maring, H., and Gao, L.: An overview of the ORACLES (ObseRvations of Aerosols above CLouds and their intEractionS) project: aerosol-cloud-radiation interactions in the Southeast Atlantic basin, Atmos. Chem. Phys. Disc., 2020, 1–82, https://doi.org/10.5194/acp-2020-449, 2020.

Robinson, N. F. and Lamb, D.: Technical Note: On the Calibration of an Opticle Particle Counter, Aerosol Sci. Tech., 5, 113–116, https://doi.org/10.1080/02786828608959081, 1986.

Rosenberg, P. D., Dean, A. R., Williams, P. I., Dorsey, J. R., Minikin, A., Pickering, M. A., and Petzold, A.: Particle sizing calibration with refractive index correction for light scattering optical particle counters and impacts upon PCASP and CDP data collected during the Fennec campaign, Atmos. Meas. Tech., 5, 1147–1163, https://doi.org/10.5194/amt-5-1147-2012, 2012.

Saleh, R., Hennigan, C. J., McMeeking, G. R., Chuang, W. K., Robinson, E. S., Coe, H., Donahue, N. M., and Robinson, A. L.: Absorptivity of brown carbon in fresh and photo-chemically aged biomass-burning emissions, Atmos. Chem. Phys., 13, 7683–7693, https://doi.org/10.5194/acp-13-7683-2013, 2013.

Sawamura, P., Moore, R. H., Burton, S. P., Chemyakin, E., Müller, D., Kolgotin, A., Ferrare, R. A., Hostetler, C. A., Ziemba, L. D., Beyersdorf, A. J., and Anderson, B. E.: HSRL-2 aerosol optical measurements and microphysical retrievals vs. airborne in situ measurements during DISCOVER-AQ 2013: an intercomparison study, Atmos. Chem. Phys., 17, 7229–7243, https://doi.org/10.5194/acp-17-7229-2017, 2017.

Schwarz, J. P., Gao, R. S., Fahey, D. W., Thomson, D. S., Watts, L. A., Wilson, J. C., Reeves, J. M., Darbeheshti, M., Baumgardner, D. G., Kok, G. L., Chung, S. H., Schulz, M., Hendricks, J., Lauer, A., Kärcher, B., Slowik, J. G., Rosenlof, K. H., Thompson, T. L., Langford, A. O., Loewenstein, M., and Aikin, K. C.: Single-particle measurements of midlatitude black carbon and light-scattering aerosols from the boundary layer to the lower stratosphere, J. Geophys. Res.–Atmos., 111, https://doi.org/10.1029/2006JD007076, 2006.

Sedlacek, III, A. J., Buseck, P. R., Adachi, K., Onasch, T. B., Springston, S. R., and Kleinman, L.: Formation and evolution of tar balls from northwestern US wildfires, Atmos. Chem. Phys., 18, 11 289–11 301, https://doi.org/10.5194/acp-18-11289-2018, 2018a.

Sedlacek, III, A. J., Onasch, T. B., Nichman, L., Lewis, E. R., Davidovits, P., Freedman, A., and Williams, L.: Formation of refractory black carbon by SP2-induced charring of organic aerosol, Aerosol Science and Technology, 52, 1345–1350, https://doi.org/10.1080/02786826.2018.1531107, 2018b.

Shinozuka, Y., Saide, P. E., Ferrada, G. A., Burton, S. P., Ferrare, R., Doherty, S. J., Gordon, H., Longo, K., Mallet, M., Feng, Y., Wang, Q., Cheng, Y., Dobracki, A., Freitag, S., Howell, S. G., LeBlanc, S., Flynn, C., Segal-Rosenhaimer, M., Pistone, K., Podolske, J. R., Stith, E. J., Bennett, J. R., Carmichael, G. R., da Silva, A., Govindaraju, R., Leung, R., Zhang, Y., Pfister, L., Ryoo, J.-M., Redemann, J., Wood, R., and Zuidema, P.: Modeling the smoky troposphere of the southeast Atlantic: a comparison to ORACLES airborne observations from September of 2016, Atmos. Chem. Phys., 20, 11 491–11 526, https://doi.org/10.5194/acp-20-11491-2020, 2020.

Shiraiwa, M., Ueda, K., Pozzer, A., Lammel, G., Kampf, C. J., Fushimi, A., Enami, S., Arangio, A. M., Fröhlich-Nowoisky, J., Fujitani, Y., Furuyama, A., Lakey, P. S. J., Lelieveld, J., Lucas, K., Morino, Y., Pöschl, U., Takahama, S., Takami, A., Tong, H., Weber, B., Yoshino, A., and Sato, K.: Aerosol Health Effects from Molecular to Global Scales, Environ. Sci. Technol., 51, 13 545–13 567, https://doi.org/10.1021/acs.est.7b04417, 2017.

Stolzenburg, M., Kreisberg, N., and Hering, S.: Atmospheric Size Distributions Measured by Differential Mobility Optical Particle Size Spectrometry, Aerosol Sci. Tech., 29, 402–418, https://doi.org/10.1080/02786829808965579, 1998.

Sumlin, B. J., Heinson, W. R., and Chakrabarty, R. K.: Retrieving the aerosol complex refractive index using PyMieScatt: A Mie computational package with visualization capabilities, J. Quant. Spectrosc. Ra., 205, 127 – 134, https://doi.org/10.1016/j.jqsrt.2017.10.012, 2018a.

Sumlin, B. J., Heinson, Y. W., Shetty, N., Pandey, A., Pattison, R. S., Baker, S., Hao, W. M., and Chakrabarty, R. K.: UV–Vis–IR spectral complex refractive indices and optical properties of brown carbon aerosol from biomass burning, J. Quant. Spectrosc. Ra., 206, 392 – 398, https://doi.org/10.1016/j.jqsrt.2017.12.009, 2018b.

Twomey, S.: The Influence of Pollution on the Shortwave Albedo of Clouds, J. Atmos. Sci., 34, 1149–1152, https://doi.org/10.1175/1520-0469(1977)034<1149:TIOPOT>2.0.CO;2, 1977.

van de Hulst, H. C.: Light Scattering by Small Particles, Wiley, 1957.

Volkamer, R., Baidar, S., Campos, T. L., Coburn, S., DiGangi, J. P., Dix, B., Eloranta, E. W., Koenig, T. K., Morley, B., Ortega, I., Pierce, B. R., Reeves, M., Sinreich, R., Wang, S., Zondlo, M. A., and Romashkin, P. A.: Aircraft measurements of BrO, IO, glyoxal, NO_2, H_2O, O_2–O_2 and aerosol extinction profiles in the tropics: comparison with aircraft-/ship-based in situ and lidar measurements, Atmos. Meas. Tech., 8, 2121–2148, https://doi.org/10.5194/amt-8-2121-2015, 2015.

Wang, X.: Optical particle counter (OPC) measurements and pulse height analysis (PHA) data inversion, Ph.D. thesis, University of Minnesota, 2002.

Whitby, K. T. and Vomela, R. A.: Response of single particle optical counters to nonideal particles, Environ. Sci. Technol., 1, 801–814, https://doi.org/10.1021/es60010a002, 1967.

Wickramasinghe, N. C.: Light Scattering Functions for Small Particles: With Applications in Astronomy, Hilger, 1973.

Woodcock, A. H.: Note Concerning Human Respiratory Irritation Associated with High Concentrations of Plankton and Mass Mortality of Marine Organisms, J. Mar. Res., 7, 56–62, 1948.

Yang, M., Howell, S. G., Zhuang, J., and Huebert, B. J.: Attribution of aerosol light absorption to black carbon, brown carbon, and dust in China – interpretations of atmospheric measurements during EAST-AIRE, Atmos. Chem. Phys., 9, 2035–2050, https://doi.org/10.5194/acp-9-2035-2009, 2009.

Yokelson, R. J., Burling, I. R., Urbanski, S. P., Atlas, E. L., Adachi, K., Buseck, P. R., Wiedinmyer, C., Akagi, S. K., Toohey, D. W., and Wold, C. E.: Trace gas and particle emissions from open biomass burning in Mexico, Atmos. Chem. Phys., 11, 6787–6808, https://doi.org/10.5194/acp-11-6787-2011, 2011.

Zhang, S.-H., Akutsu, Y., Russell, L. M., Flagan, R. C., and Seinfeld, J. H.: Radial Differential Mobility Analyzer, Aerosol Sci. Tech., 23, 357–372, https://doi.org/10.1080/02786829508965320, 1995.

Zhou, J.: Hygroscopic Properties of Atmospheric Aerosol Particles in Various Environments, Ph.D. thesis, Department of Nuclear Physics, Lund University, 2001.